

Thermal chiral anomaly in the magnetic-field-induced ideal Weyl phase of Bi_{1-x}Sb_x

Dung Vu¹, Wenjuan Zhang², Cüneyt Şahin^{3,4}, Michael E. Flatté^{3,4}, Nandini Trivedi² and Joseph P. Heremans^{1,2,5} □

The chiral anomaly is the predicted breakdown of chiral symmetry in a Weyl semimetal with monopoles of opposite chirality when an electric field is applied parallel to a magnetic field. It occurs because of charge pumping between monopoles of opposite chirality. Experimental observation of this fundamental effect is plagued by concerns about the current pathways. Here we demonstrate the thermal chiral anomaly, energy pumping between monopoles, in topological insulator bismuth-antimony alloys driven into an ideal Weyl semimetal state by a Zeeman field, with the chemical potential pinned at the Weyl points and in the absence of any trivial Fermi surface pockets. The experimental signature is a large enhancement of the thermal conductivity in an applied magnetic field parallel to the thermal gradient. This work demonstrates both pumping of energy and charge between the two Weyl points of opposite chirality and that they are related by the Wiedemann-Franz law.

aterials whose electrons are described by relativistic equations of motion for gravitational forces and electron dynamics¹ are Weyl semimetals (WSMs). The chiral anomaly was predicted² to be an experimental signature for the existence of WSMs. Its importance extends beyond solid-state physics: it provides a mechanism for charge-parity violation³ and the matter/antimatter imbalance in the universe; in condensed-matter materials, the analogous quasiparticle non-conservation is connected with a change in the vacuum state, thus preserving overall electron number.

Previous experimental determination methods for the chiral anomaly are tainted. First, currently investigated WSMs^{4–6} are not ideal; their Fermi surfaces contain features other than Weyl nodes. Second, the signature chiral anomaly feature is a negative longitudinal magnetoresistance (MR);⁷ however the distorted current lines in the applied magnetic field complicate the interpretation.

Ideal WSMs have two distinguishing characteristics. First, the band structure has linearly dispersing bands that intersect at Weyl points (WPs) in a system that breaks time reversal symmetry (TRS) or inversion symmetry. Second, the electrochemical potential μ is at the WP energy ($\mu\!=\!0$). In an ideal WSM, there are no trivial bands at the energy μ , which is pinned to the WPs. Then, the Fermi surface consists only of WPs with opposite Berry curvatures, W_R right-handed or W_L left-handed. One pair of WPs in the Brillouin zone (BZ) is the minimum required by the Nielsen–Ninomiya theorem² for a TRS-breaking ideal WSM. Experimentally, an ideal WSM displays no Shubnikov–de Haas (SdH) oscillations; at finite temperature, a nearly equal density of intrinsic holes and electrons is excited thermally, with any unbalance due to unintentional doping smaller than this intrinsic concentration.

The chiral anomaly² in ideal WSMs results from applying parallel electric, **E**, and magnetic, **B**, fields along the direction of the WP separation. **B** separates the bands into Landau levels (LL), with a two-dimensional density of states (DOS) proportional to $1/\ell_B^2$, where $\ell_B \equiv \sqrt{\hbar/eB}$ is the magnetic length (e is the electron charge

and \hbar is the Planck's constant). The chirality $(\chi=\pm 1)$ dictates that in the extreme quantum limit (EQL), when only the last LL is populated, electrons have only one Fermi velocity per WP: W_R ($\chi=+1$) has only right-moving electrons of velocity ν ; W_L ($\chi=-1$) only left movers of velocity $-\nu$. E shifts the electron momentum in the last LL by $\delta k \propto eE\tau$ (τ^{-1} is the inter-WP scattering rate). This generates right movers by an amount $\delta n_{+1} \propto \delta k_{+1}/\ell_B^2 \propto E\tau/\ell_B^2$ and annihilates left movers by an amount $\delta n_{-1} \propto -E\tau/\ell_B^2$. This particle generation/annihilation process is the chiral anomaly, giving rise to an additional electric current proportional to ν and $\delta n_{+1} - \delta n_{-1}$, which is proportional to E=|E| and $|B|=\mu_0H$ both applied along the z direction (μ_0 is the vacuum permeability). The anomalous contribution to the electrical conductivity generated by N_w degenerate pairs of WPs is:⁷

$$\sigma_{zz} = N_{\rm w} \frac{e^2 v \tau}{4\pi \hbar \ell_B^2} = N_{\rm w} \frac{e^3 v \tau}{4\pi \hbar^2} B_z \tag{1}$$

The scientific community considers the resulting negative longitudinal MR to be the crucial experimental chiral anomaly signature^{4,5,7,8}.

Negative MR was observed in many WSMs, for example, XPn compounds (X=Nb, Ta; Pn=As, Sb)⁴⁻⁶ and Dirac semimetals⁸⁻¹¹, but also in materials without Weyl points near μ , for example, XPn₂ compounds¹²⁻¹⁵ and elemental semimetal Bi (ref. ⁸). Broadly observing this effect revealed that the negative MR is unlikely to be a unique chiral anomaly signature: other, classical effects might be present, as discussed next^{16,17}.

The classical effects that make longitudinal MR measurements ambiguous arise because the Lorentz force distorts the current flow spatial distribution in samples with high-mobility (μ_B) electrons under a magnetic field (that is, when $\mu_B|\mathbf{B}|>1$). This causes extrinsic, geometry-dependent MR mechanisms. The first is 'current jetting' 8,12,17-19, arising in four-contact measurements. With $\mathbf{B}//\mathbf{E}$, the Lorentz force concentrates the current in a cyclotron motion near

¹Department of Mechanical and Aerospace Engineering, The Ohio State University, Columbus, OH, USA. ²Department of Physics, The Ohio State University, Columbus, OH, USA. ³Optical Science and Technology Center and Department of Physics and Astronomy, The University of Iowa, Iowa City, IA, USA. ⁴Pritzker School of Molecular Engineering, University of Chicago, Chicago, IL, USA. ⁵Department of Material Science and Engineering, The Ohio State University, Columbus, OH, USA. [™]e-mail: heremans.1@osu.edu

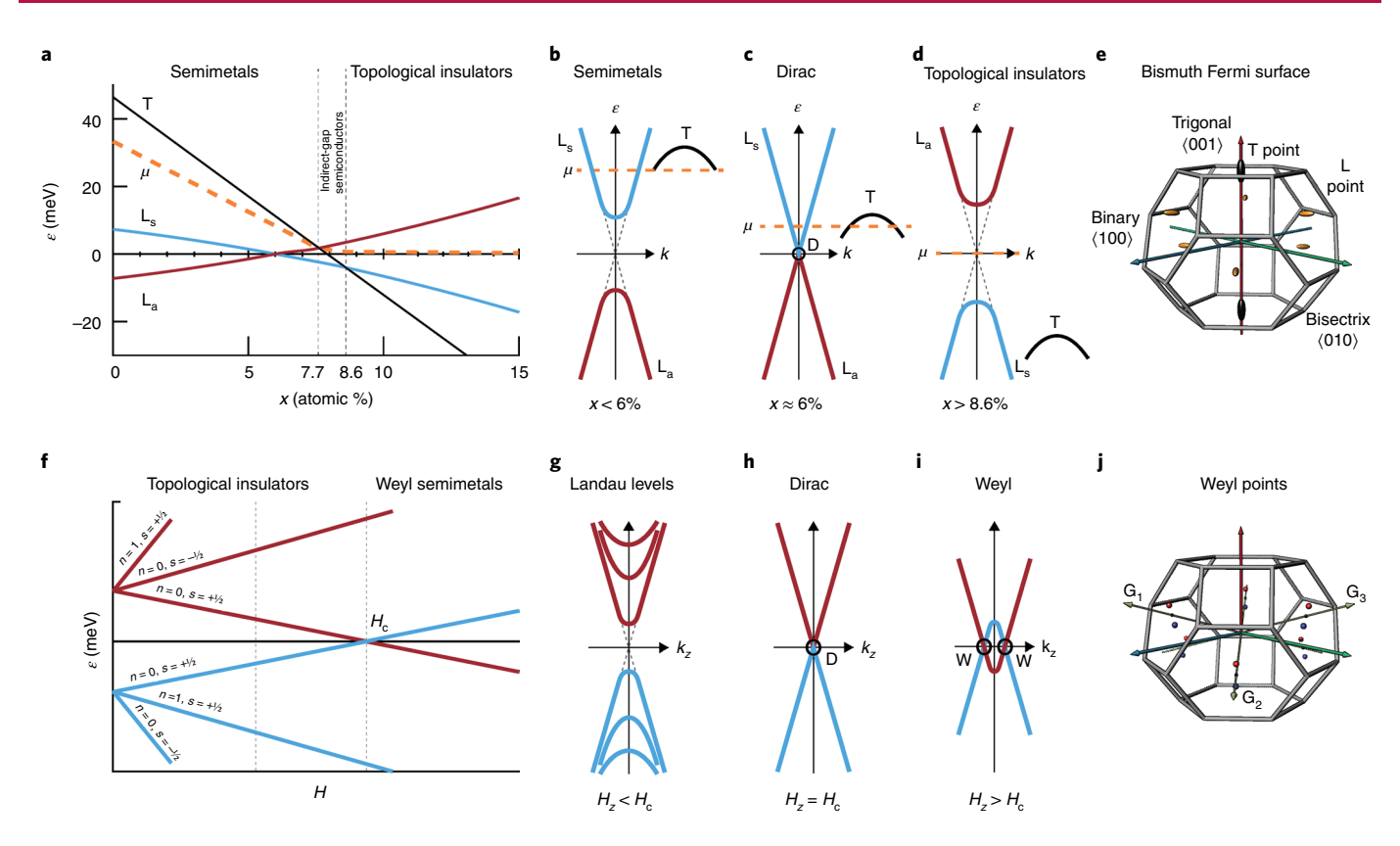


Fig. 1 [Evolution of Bi_{1-x}Sb_x alloys with composition and magnetic field. **a**, Dependence of band-edge energies (ε) on composition (x) at zero applied magnetic field. Elemental semimetal Bi has electrons residing in a conduction band, L_s, and holes in a valence band, T; with a filled second valence band, L_a. Adding Sb (x in at.%), the L_a-L_s gap closes until the bands intersect near $x \approx 6\%$. The T-band edge intersects that of the L_a and L_s bands at $x \approx 7.7\%$ and $x \approx 8.6\%$, respectively (from the virtual crystal approximation, see text). The chemical potential $\mu(x)$ evolution for samples with no unintentional doping is shown as a dashed orange line. Alloys with x < 7.7% are semimetals with μ in a band; alloys with x > 8.6% are direct-gap Tls³¹ with μ at mid-gap in undoped material. **b**, Semimetal Bi dispersion relationship. **c**,**d**, Dirac dispersion of Bi₉₄Sb₆ alloys (**c**) and dispersion of Bi-Sb Tls (**d**). **e**, Bi BZ and Fermi surfaces: electrons fill six pockets at the BZ L-points; holes fill two pockets at the T-points. **f**, Tl alloy Bi₈₉Sb₁₁ band-edge energies in a magnetic field H_2 applied along the trigonal direction. The field separates the L_a and L_s valence bands into Landau levels, with orbital quantum number n and spin s. With increasing n is n to n and n spands cross again at a critical field n the n and n spands cross again at a critical field n becomes that of a field-induced Weyl semimetal. **j**, Bi_{1-x}Sb_x BZ with locations of calculated WPs shown schematically; blue and red points indicate WPs with opposite Berry curvature.

the sample centre. Progressively less current passes near the voltage probes as **B** increases, lowering the measured voltage and possibly leading to the erroneous conclusion that the resistivity decreases with B. The second is an extrinsic 'positive geometrical MR' arising if B is slightly misaligned with respect to the current flow lines¹⁶. In the present samples, striations present on the surface of a Czochralski-grown crystal²⁰ can overwhelm the MR measurements, and extreme care needs to be taken with the sample alignment and geometry (see Supplementary Information). Samples with reduced cross-section and smooth edges minimize both effects. Thermal conductivity $\kappa_{zz}(H_z)$ measurements with the heat flux and the magnetic field along the z direction (H_z) avoid problems with extrinsic MR because there is no external current flow and the lattice contribution to κ maintains a more **B**-independent heat flux than charge flux distribution in the sample. There is a magnetic field effect on anharmonic phonon scattering²¹, but it is an order of magnitude smaller than the effects discussed here.

Energy transport in WSMs poses new theoretical challenges. From the equations of motion for charge carriers at the WP and the Boltzmann transport equation, we write the imbalance between left- and right-moving particles (δn_{χ}) and energy $(\delta \varepsilon_{\chi})$, the thermal chiral anomaly) in the presence of both an electric field E and thermal gradient $\nabla_{\tau} T$ as:²²

$$\delta n_{\chi} = \frac{\chi e^{2} \tau}{4\pi^{2} \hbar^{2}} \left[\mathbf{B} \cdot \mathbf{E} \right] C_{0} + \frac{\chi e \tau}{4\pi^{2} \hbar^{2}} \left[\mathbf{B} \cdot \frac{-\nabla_{r} T}{T} \right] C_{1}$$
 (2)

$$\delta\epsilon_{\chi} = \frac{\chi e^{2}\tau}{4\pi^{2}\hbar^{2}} \left[\mathbf{B} \cdot \mathbf{E} \right] \left(\mu C_{0} + C_{1} \right) + \frac{\chi e\tau}{4\pi^{2}\hbar^{2}} \left[\mathbf{B} \cdot \frac{-\nabla_{r}T}{T} \right] \left(\mu C_{1} + C_{2} \right)$$
(3)

where $C_m = \int (\epsilon - \mu)^m \left(-\partial f_0/\partial \epsilon \right) d\epsilon$, $m \in \{0, 1, 2...\}$ with f_0 the Fermi–Dirac distribution function. The thermal chiral anomaly thus has two terms. First, a temperature gradient $\nabla_r T$ alone, disregarding any induced electric field, creates an imbalance between the energy carried by the left and right movers while maintaining equal populations when $\mu = 0$ ($C_1 = 0$, $\delta n_\chi = 0$, $\delta \epsilon_\chi \neq 0$). This response contrasts with the electrical case, where $\nabla_r T = 0$, and \mathbf{E} creates an imbalance between the populations of left and right movers while, when $\mu = 0$, maintaining the same total energy $(\delta n_\chi \neq 0, \ \delta \epsilon_\chi = 0)$. Second, when the sample is mounted in open-circuit conditions and no external electric field is applied, applying $\nabla_r T$ induces a Seebeck electric field $\mathbf{E} = S(-\nabla_r T)$ (S is the thermopower), driving both $\delta n_\chi \neq 0$ and $\delta \epsilon_\chi \neq 0$. This creates an additional $\kappa_{zz}(H_z)$ term, the ambipolar thermal conductivity²³, $S^2 T \sigma$ (see Supplementary Information). The total thermal

NATURE MATERIALS ARTICLES

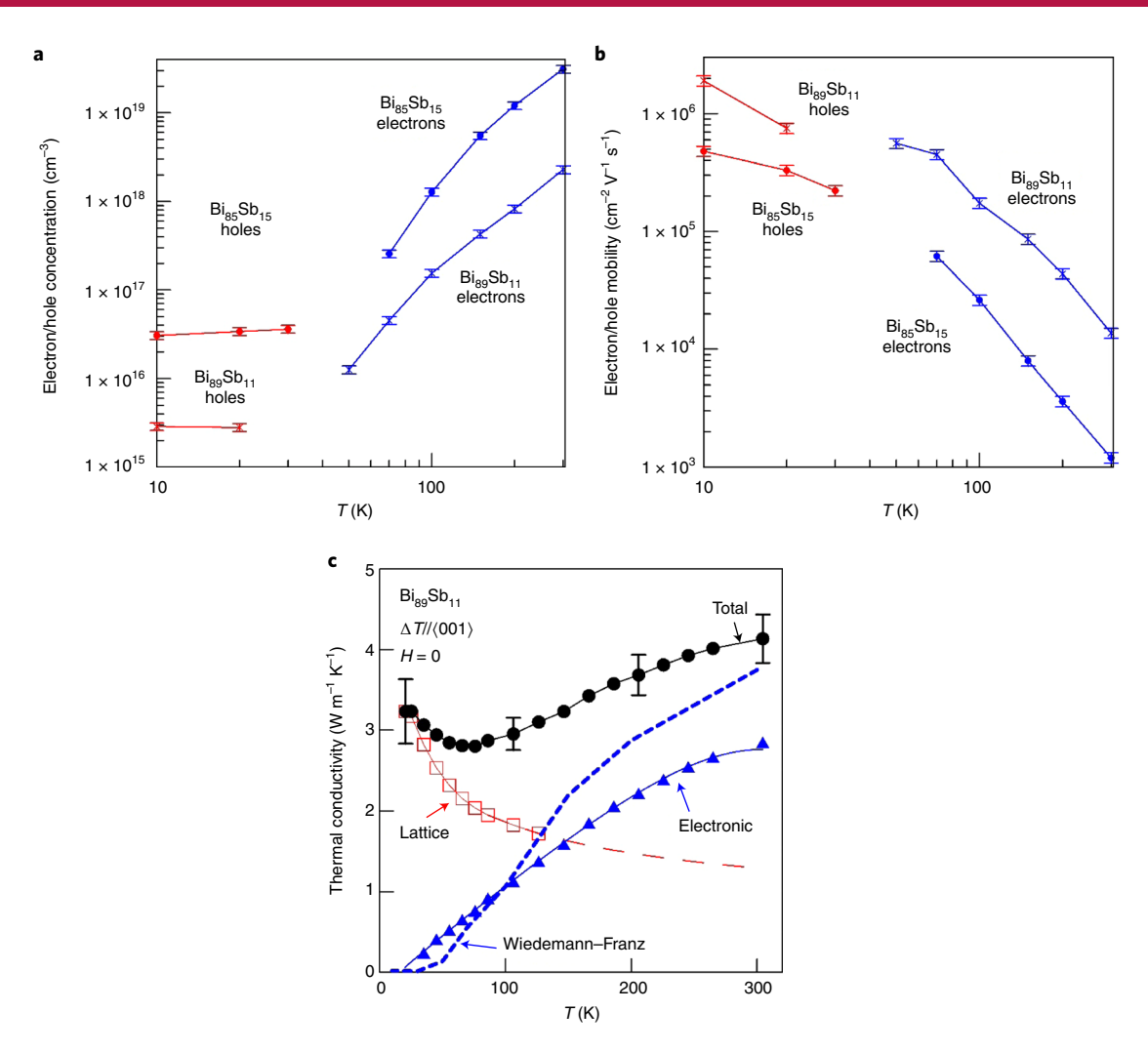


Fig. 2 | $\mathbf{Bi}_{89}\mathbf{Sb}_{13}$ and $\mathbf{Bi}_{85}\mathbf{Sb}_{15}$ electronic and thermal properties versus temperature (T). \mathbf{a} , \mathbf{b} , Carrier concentration (\mathbf{a}) and mobility (\mathbf{b}); the samples switch from dominantly n-type at 300 K to dominantly p-type at 10 K. \mathbf{c} , $\mathbf{Bi}_{89}\mathbf{Sb}_{11}$ zero-field κ_{22} (z denotes the <001> crystallographic direction) separated into lattice κ_L and electronic κ_E parts (see Supplementary Information for $\mathbf{Bi}_{85}\mathbf{Sb}_{15}$ data). The dashed blue line is κ_E calculated from the resistivity and the Wiedemann-Franz law with $L=L_0$. The error bars are standard deviations and their origins are described in the Methods.

conductivity becomes $\kappa_{zz} = \kappa_{zz,0} + S^2 \sigma T$, where $\kappa_{zz,0}$ denotes the energy carried directly by the charge carrier.

The experimental tests for these theories are first to observe an increase in electronic thermal conductivity in a longitudinal magnetic field, and second to verify the Wiedemann–Franz law (WFL) in the EQL:

$$\kappa_{zz} = LT\sigma_{zz},\tag{4}$$

with L being the Lorenz ratio. If each electron carries charge e and entropy $k_{\rm B}$, and conserves its energy during scattering, $L=L_0=\pi^2/3~(k_{\rm B}/e)^2$. The experiment consists of testing the ratio $\kappa_{zz}/T\sigma_{zz}$, which we define as L, against the independent variables H_z and T, and, if L is independent of these, to verify if the value equals L_0 . In particular, a Weyl semimetal in which inelastic scattering is limited by the inter-WP scattering time, τ , in the quasi-classical limit at H=0 is expected to have $L=7\pi^2/5~(k_{\rm B}/e)^2$, but $L=L_0$ in the EQL (see Supplementary Information and ref. ²⁴). In the presence of ambipolar conduction $L>L_0$, because L_0 applies only to $\kappa_{zz,0}$. Extrinsic effects result in underestimations (current jetting) or overestimations (geometrical MR) of L.

We report the thermal conductivity $\kappa_{zz}(H_z)$ dependence on H_z , and show experimentally that the chiral anomaly affects energy and charge

transport similarly, that is, $d\kappa_{zz}/dH_z > 0$, as expected from equations (1) and (4). We then experimentally derive values for L. Previous $\kappa_{zz}(H_z)$ measurements exist: an increase in κ_{zz} for GdPtBi has been reported at $H_z = 9 \text{ T}$ (ref. ²⁵). However, those samples exhibited SdH oscillations in their MR, which proves that μ is not at the WPs, and the increase in κ_{zz} is also observed in a transverse field, which is difficult to reconcile with Weyl physics. A positive magnetothermoelectric conductance is observed in NbP26, dubbed a gravitational anomaly due to the formal link^{27,28} between gradients $abla {m \Phi}$ in the gravitational field and $\nabla_r T$. Here, we report $\kappa_{zz}(H_z)$ in magnetic-field-induced ideal WSMs, $Bi_{1-x}Sb_x$ alloys with x=11 and 15 at.%. We demonstrate that these alloy samples, topological insulators (TIs) at $|\mathbf{B}| = 0$ (ref. 29), become WSMs without trivial bands in a quantizing magnetic field along the trigonal axis (z = <0.01>). We further identify the WP locations. In these material samples, we show their carrier concentrations are intrinsic above ~30 K, where the relevant κ_{zz} data are collected. This makes them ideal WSMs by construction. Their $\kappa_{zz}(H_z)$ shows an electronic thermal conductivity increase of up to 300% at 9 T. Lorenz ratio measurements, $L = \kappa_{zz}/T\sigma_{zz}$, show that $L \approx L_0$. We show that the effect is robust to disorder and phonon scattering, depends as expected on the ratio of the temperature to the Weyl bandwidths and is absent in samples that fall outside the range of compositions where WSMs form in an applied magnetic field.

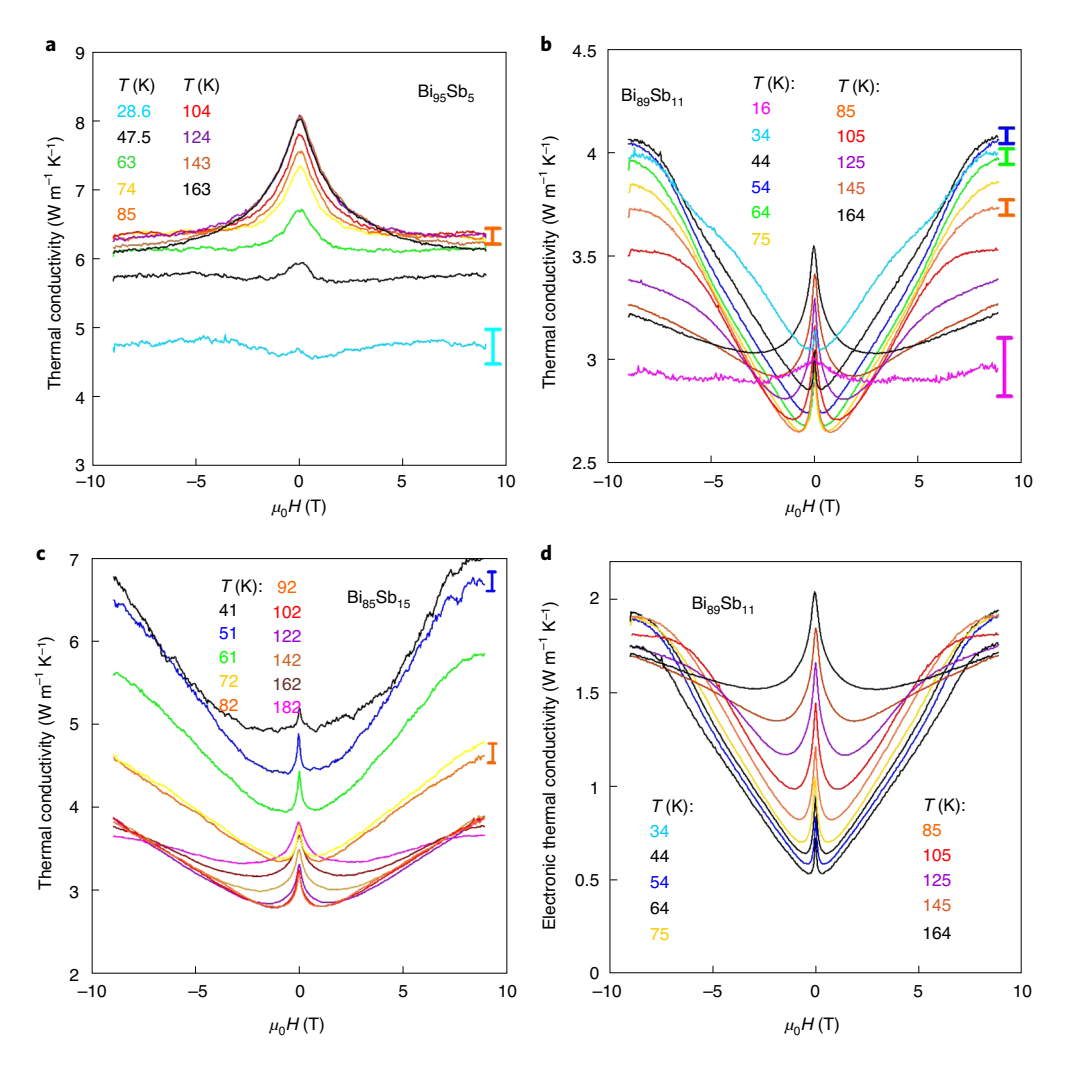


Fig. 3 | $Bi_{98}Sb_{5}$, $Bi_{89}Sb_{11}$ and $Bi_{85}Sb_{15}$ thermal conductivity $\kappa_{zz}(H_z)$ dependence on longitudinal magnetic field (*H*) along the trigonal (z = <001>) direction at temperatures indicated. a, $Bi_{98}Sb_{5}$, a conventional, not Weyl, semimetal has $\kappa_{zz}(H_z)$ that monotonically decreases with H_z , due to a positive MR. **b,c**, The $\kappa_{zz}(H_z)$ of $Bi_{89}Sb_{11}$ (sample 1) (**b**) and $Bi_{85}Sb_{15}$ (**c**) shows a decrease due to a conventional positive MR in the TI regime, followed by an increase that we posit is evidence for the thermal chiral anomaly. **d**, The electronic contribution κ_E of the total thermal conductivity κ_{zz} for $Bi_{89}Sb_{11}$ is obtained by subtracting the lattice contribution κ_L shows an increase as large as 300% with field at 9 T. The error bars, the standard deviation relative to the field dependence, are obtained as described in the Methods. They are temperature dependent and are the same for all samples at the same temperatures.

Magnetic-field-induced Bi_{1-x}Sb_x Weyl semimetals

We predict that $\mathrm{Bi}_{1-x}\mathrm{Sb}_x$ alloys ($\sim 9 < x < \sim 18$ at.%) become ideal WSMs in a magnetic field, H_z , above a critical threshold H_C because: (1) their conduction and valence bands cross at H_C ; (2) at $H_z > H_C$ two crossing points appear that are Berry curvature monopoles, or WPs; and (3) no trivial bands cross μ .

The band structure of $\mathrm{Bi_{1_x}Sb_x}$ alloys (Fig. 1a–e) at zero magnetic field evolves with increasing x through four successive regimes: onventional semimetals, semimetals with an inverted band at the BZ L-point, indirect-gap semiconductors and direct-gap TIs. A tight-binding Hamiltonian describes the band structure of unalloyed bismuth and antimony incorporating the s and p orbitals of the two atoms in the conventional hexagonal unit cell. The alloy electronic structure is calculated (see Supplementary Information) using a modified virtual crystal approximation in which the tight-binding parameters are obtained directly from those of the elemental semimetals and agree with previous experiments $^{32-34}$ within the experimental uncertainty on compositions (1 at.%). The details of the electronic structure of the Bi–Sb alloy change slowly as the band positions change relative to μ , as indicated by the nearly unchanged intrinsic spin-Hall conductivity calculated through the semimetal–TI transitions 35 .

With these parameters, we show that a quantizing magnetic field along the trigonal direction of the TIs (Fig. 1f-i) inverts the bands again. The g_{eff}-tensors at the high-symmetry BZ L- and T-points are calculated36 from the tight-binding electronic structure above for valence and conduction bands. The T-point g_{eff} -tensor has only one non-zero component, $g_{hz} = 20.5$, which only couples to the magnetic field along z. The more complicated effective g_{eff} -tensor at the L-point shows substantial asymmetry. For the conduction and valence bands at the Bi₈₉Sb₁₁ L-point with a magnetic field applied along the trigonal direction, the calculated values are $g_z = -77.5$ and -72.3, respectively. SdH oscillations³⁷ in Bi confirm the extremely large g-factor values experimentally. This results in an anomalously large effective Zeeman splitting energy $\Delta \epsilon_z = -\mu_B g_z B_z \approx -4.2 \, \text{meV T}^{-1}$ at the L-point that overwhelms the orbital splitting of the LLs. Consequently, the band gaps close (Fig. 1f,h) at a critical field H_C which is calculated to be ~3 T for alloy compositions near x = 11%. Magnetic-field-induced band closings are uncommon, but have been reported via magneto-optical measurements on Bi (ref. 38). $H_{\rm C}$ is sensitive to parameter values used in the calculations, and is of the order of 1–4 T. At $H_z > H_C$, the Zeeman energy increase further splits the degeneracy of the Kramers doublets (points W in Fig. 1i).

NATURE MATERIALS ARTICLES

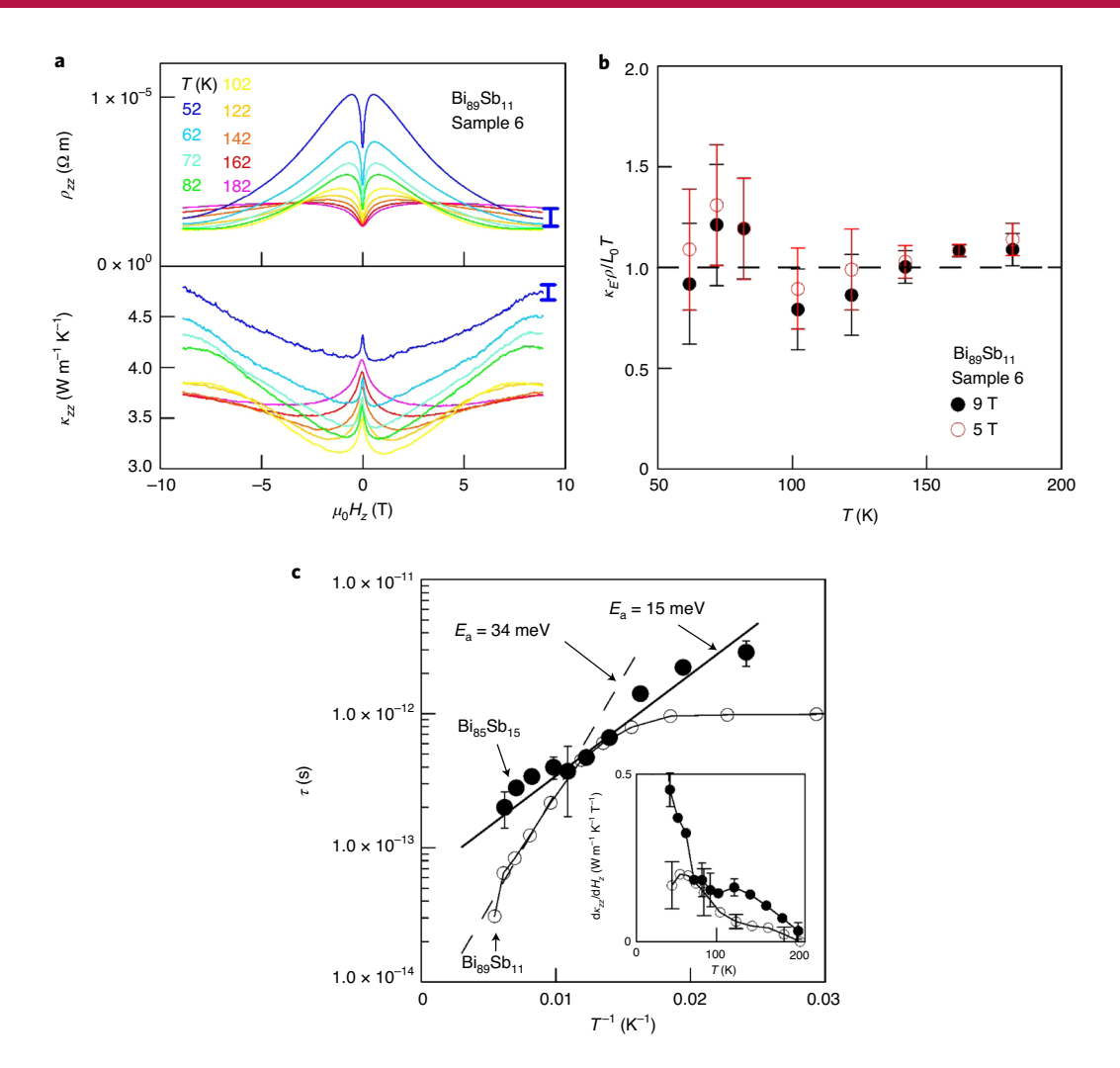


Fig. 4 | Wiedemann-Franz law verification; temperature (*T***) dependence of the** $\kappa_{zz}(H_z)$ **increase. a**, Bi₈₉Sb₁₁ (sample 6) magnetothermal conductivity $\kappa_{zz}(H_z)$ and resistivity $\rho_{zz}(H_z)$. The error bars on the resistivity and thermal conductivity are the standard deviation obtained as described in the Supplementary Information. **b**, Lorenz ratio $L = \kappa_{zz,E}(H_z)\rho_{zz}(H_z)/T$ derived from **a**, normalized to L_0T at two values of H_z ; L is independent of H_z within the error bars arise from the errors on $\rho_{zz}(H_z)$ and on $\kappa_{zz,E}(H_z)$ determined from $\kappa_{zz,E}(H_z)$ and κ_L . **c**, The inter-WP scattering time, τ , derived from equation (5) fits Arrhenius plots (lines) at T > 60 K with an activation energy of $E_a = 34$ meV for Bi₈₉Sb₁₁ and 15 meV for Bi₈₅Sb₁₅. The inset shows the temperature dependence of $d\kappa_L(H_z)/dH_z$ between 4 and 8 T of sample 1 (see Table 1) Bi₈₀Sb₁₁ and Bi₈₀Sb₁₅.

We further demonstrate that the Kramers doublets become WPs resulting from explicit TRS breaking by showing that the Chern number changes by an integer for a momentum slice taken between these WPs. The Chern number is an integer that counts the monopoles enclosed in a given Gaussian surface in the BZ.

We calculate the Berry curvature distribution $\Omega_n(\mathbf{k})$ in momentum space to search for the WPs where the Berry curvature is concentrated and singular (see Supplementary Information). The two WPs carry monopole Berry curvature $\Omega(\mathbf{k}) = \chi \mathbf{k}/k^3$ with opposite chirality, $\chi = \pm 1$ (Supplementary Fig. 3.1). Integrating the Berry curvature provides the Chern number (see Supplementary Information). A Chern number integer change provides evidence of a topology change and existence of WPs, a pair of points separated symmetrically near each L-point in the three-dimensional BZ (Fig. 1j). The separation between the two WPs is in the binary-trigonal plane with a major component along the trigonal direction (coinciding with the external magnetic field direction) and a minor component along the bisectrix direction.

Finally, to ascertain that the $Bi_{89}Sb_{11}$ system is an ideal WSM at $H_z > H_C$, the model verifies that no trivial bands contribute to

transport: neither the T-point band nor any new bands move near μ with increasing H_z . In a semiconductor or semimetal without unintentional doping, μ is pinned at the energy of the lowest DOS, which, without trivial bands, occurs at the WPs. Therefore, if we can minimize unintentional doping, our experimental systems will form ideal WSMs by construction.

Magnetothermal conductivity measurements

Evidence for the thermal chiral anomaly is shown in six single-crystal samples of $\mathrm{Bi}_{1-x}\mathrm{Sb}_x$, with $x\!\approx\!11$ and 15 at.%. For control, we report the absence of the anomaly in two semimetallic samples with $x\!\approx\!5\%$; for this composition an ideal WSM does not exist. The sample compositions and characterizations are presented in Table 1 and explained in the Methods. The temperature dependence of the resistivity and low-field Hall effect of the best samples (sample 1 with $x\!=\!11\%$ and $x\!=\!15\%$) are used to derive carrier concentration and mobility (Fig. 2a,b) showing that charge carriers freeze out. This, and the absence of SdH oscillations in the high-field longitudinal magnetoresistivity down to 2 K and other transport properties (Supplementary Information), indicate that

Table 1 Samples used in this study					
Sample name	Growth	x (at.%)	Used for	Density (cm ⁻³)	Mobility (cm ² V ⁻¹ s ⁻¹)
Sample 1	TMZ	10.5 ± 0.5	$\kappa_{zz}(H_z)$, $\kappa_{zz}(H_y)$ $\kappa_{zz}(H_z)$ Ag contacts		
Hall	TMZ	10.5 ± 0.5	Hall, resistivity	3×10 ¹⁵ (10 K)	1.9×10 ⁶ (10 K)
Sample 2	Czochralski	11.3 ± 0.7	Negative MR		
		11.3 ± 0.7	Magneto-Seebeck		
		11.3 ± 0.7	$\kappa_{zz}(H_z)$, $\kappa_{zz}(H_y)$		
Sample 3	Czochralski	11.3 ± 0.7	$\kappa_{zz}(H_z)$, $\kappa_{zz}(H_y)$		
		11.3 ± 0.7	$\kappa_{zz}(H_z)$ -angular dependence		
Sample 4	Czochralski	11.3 ± 0.7	$\kappa_{zz}(H_z)$, $\kappa_{zz}(H_y)$		
Hall	Czochralski	11.3 ± 0.7	Hall, resistivity	1.4×10^{16} (12 K)	2×10 ⁴ (12K)
Sample 5	TMZ	15.1 ± 0.7	$\kappa_{zz}(H_z)$, $\kappa_{zz}(H_y)$		
Hall	TMZ	15.1 ± 0.7	Hall, resistivity	$3 \times 10^{16} (10 \text{ K})$	4.5×10^{5} (10 K)
Sample 6	TMZ	10.5 ± 0.5	$\kappa_{zz}(H_z), \rho_{zz}(H_y)$	As sample 1	As sample 1
Semimetal	Bridgeman	5 ± 0.5	$\kappa_{zz}(H_z) \kappa_{zz}(H_z)$ Ag contacts, Hall, resistivity	4.5×10 ¹⁶ (79 K)	8×10 ⁴ (79 K)

they are ideal WSMs. The zero-field thermal conductivity κ_{zz} along the trigonal direction of sample 1 is given in Fig. 2c (for x=15%, Supplementary Information). It consists of a phonon κ_L and electronic κ_E contribution separated by measuring $\kappa_{zz}(H_y)$ (index y denotes the <010> crystallographic direction) (Supplementary Information), which shows a steady decrease to a saturation value at high field. This is the ordinary behaviour of high-mobility materials^{39,40} used to isolate $\kappa_L = \lim_{H_y \to \infty} (\kappa_{zz}(H_y))$ for T<120 K. For T>120 K, $\kappa_L(T)$ is extrapolated following a $T^{-1/3}$ law⁴¹ to 300 K. κ_L dominates κ_{zz} below 35 K, limiting measurements of κ_E to T>35 K. At zero field, κ_E (H_z =0) follows the WFL with L= L_0 (dashed line in Fig. 2c) above 35 K.

Figure 3 shows the longitudinal magnetothermal conductivity $\kappa_{zz}(H_z)$ of three samples: Bi₉₅Sb₅ (not a WSM); Bi₈₉Sb₁₁ and Bi₈₅Sb₁₅ (both WSMs above 1–2 T). $\kappa_{\rm E}(H_z)$ of ${\rm Bi}_{89}{\rm Sb}_{11}$ is reported as a function of H_z in Fig. 3d: the relative κ_E increase in magnetic field reaches above 300% from 34 to 85 K at 9 T. At low field, $d\kappa_{zz}/dH_z < 0$ for H_z <1T at T<50K and H_z <3T at T=160K. Here, the last LLs of the conduction and valence bands have not crossed in energy. At high field, in WSM phase, $d\kappa_{zz}/dH_z > 0$. The dependence of the effect on the angle between ∇T and H is given in the Supplementary Information. We posit that the large increase in $\kappa_{zz}(H_z)$ (Fig. 3b-d) at high field is experimental evidence for the thermal chiral anomaly. The following observations justify this thesis. First, Fig. 3a shows that $d\kappa_{zz}/dH_z < 0$ at all fields for Bi₉₅Sb₅, which in zero field is a conventional semimetal, not a TI, with a trivial hole pocket in its Fermi surface at the BZ T-point. In Bi₉₅Sb₅, the band crossing with field does not create an ideal WSM phase; if the $d\kappa_{zz}/dH_z > 0$ observation on Bi₈₉Sb₁₁ and Bi₈₅Sb₁₅ resulted from effects other than the chiral anomaly, for example, ionized impurity scattering⁴¹, known to be weak even in doped Bi (ref. 20), it also would occur in similarly prepared Bi₉₅Sb₅. Second, to ascertain that a circulating current or an artefact on the sample surfaces does not induce the effect, samples of Bi₉₅Sb₅ and Bi₈₉Sb₁₁ were mounted with their top and bottom faces covered by electrically conducting Ag epoxy (see Supplementary Information). We observe no effect from the added surface conducting layers. Third, the $d\kappa_{zz}/dH_z > 0$ data at high H_z were reproduced on Bi₈₉Sb₁₁ samples 2-4 (see Supplementary Information), which had a mobility of only 2×104 cm² V⁻¹ s⁻¹ at 12 K, demonstrating the robustness of the observations with respect to defect scattering. Fourth, $d\kappa_{zz}/dH_z > 0$ in Fig. 3b-d is observed up to 200 K, twice the bismuth Debye temperature, demonstrating the robustness of the effect to phonon scattering. The effect disappears only for $T > 200 \,\mathrm{K}$, which we demonstrate in the next section

to be due to thermal smearing of the carrier population between the WPs, independent of phonons.

Verification of the Wiedemann-Franz law and evidence for inter-Weyl point scattering

Simultaneous $\kappa_{zz}(H_z)$ and MR ($\rho_{zz}(H_z)$) measurements were taken on a specially prepared Bi₈₉Sb₁₁ sample (number 6, see Table 1 and Methods), and are shown in Fig. 4a. Subtracting $\kappa_L^{\ 40}$ (Fig. 2c) from $\kappa_{zz}(H_z)$ gives $\kappa_{zz,E}(H_z)$. Figure 4b verifies that the WFL holds in an applied field with $L \approx L_0$, as expected theoretically in an ideal WSM where the WSM phase is induced in EQL. The error bar increases with decreasing T as κ_L increasingly dominates $\kappa_{zz}(H_z)$ and becomes as large as the signal below 50 K; κ_L masks the electronic contribution completely below 35 K. This knowledge allows fitting the $d\kappa_{zz}/dH_z$ (inset in Fig. 4c) experimental temperature dependence for T > 60 K. Using equations (1) and (4) with $L = L_0$, $N_w = 12$ to derive the thermal chiral conductivity, then taking its field derivative, we obtain:

$$\mathrm{d}\kappa_{zz}/\mathrm{d}H_z = \frac{\pi e v k_B^2}{\hbar^2} T\tau. \tag{5}$$

Using the calculated $v \approx 4.5 \times 10^5 \,\mathrm{m \, s^{-1}}$ (see Supplementary Information), equation (5) can be used to derive the inter-WP scatting time $\tau(T)$ (Fig. 4c). Below $\sim 60 \,\mathrm{K}$, $\tau \approx 10^{-12} \,\mathrm{s}$ and is temperature independent for Bi₈₉Sb₁₁, one order of magnitude longer than the electron relaxation time in Bi₉₅Sb₅ at 4.2 K. This suggests a high degree of charge-transport protection. In $Bi_{85}Sb_{15}$ and at T > 60 K in $Bi_{89}Sb_{11}$, τ increases exponentially with T^{-1} , activated behaviour with an activation energy $E_a = 34 \pm 2 \text{ meV}$ for $Bi_{89}Sb_{11}$ and $E_a = 15 \pm 2 \text{ meV}$ for $Bi_{85}Sb_{15}$, as expected when the mechanism that limits τ is charge carriers being thermally excited above the Weyl band width. The calculated band width (see Supplementary Information) at 7.5 T is $E_{\text{BW}} = 35 \,\text{meV}$ for $x = 10.5 \,\text{at.}\%$ and $E_{\text{BW}} = 20 \,\text{meV}$ at 7.5 T for x = 15.1 at.%, the measured concentrations in the samples. The correspondence between E_a and E_{BW} for two compositions suggests that thermal smearing of the carrier population between the WPs is the main mechanism inhibiting the observed increase in $\kappa_{zz}(H_z)$, and that E_{BW} is the only energy scale in the observations.

Altogether, we posit that the $d\kappa_{zz}/dH_z > 0$ observation constitutes robust experimental evidence for energy pumping between opposite chirality monopoles when a thermal gradient is applied parallel to a magnetic field in an ideal WSM. This is related to the excess electrical conductivity due to the charge pumping between

NATURE MATERIALS ARTICLES

opposite chirality monopoles, the chiral anomaly and by the Wiedemann–Franz law with a Lorenz number of $\pi^2/3$ $(k_B/e)^2$. The robustness of the results with respect to defect and phonon scattering, and the identification of the Weyl band width as the only energy scale, all point to the topological origin of the data.

Online content

Any methods, additional references, Nature Research reporting summaries, source data, extended data, supplementary information, acknowledgements, peer review information; details of author contributions and competing interests; and statements of data and code availability are available at https://doi.org/10.1038/s41563-021-00983-8.

Received: 17 May 2019; Accepted: 12 March 2021; Published online: 7 June 2021

References

- 1. Weyl, H. Elektron und gravitation. Z. Phys. 53, 330-352 (1929).
- Nielsen, H. B. & Ninomiya, M. The Adler–Bell–Jackiw anomaly and Weyl fermions in a crystal. *Phys. Lett.* 130B, 389–396 (1983).
- Christenson, J. H., Cronin, J. W., Fitch, V. L. & Turlay, R. Evidence for the 2π decay of the K,⁰ meson. Phys. Rev. Lett. 13, 138–140 (1964).
- Arnold, F. et al. Negative magnetoresistance without well-defined chirality in the Weyl semimetal TaP. Nat. Commun. 7, 116157 (2016).
- Huang, X. et al. Observation of the chiral-anomaly-induced negative magnetoresistance in 3D Weyl semimetal TaAs. *Phys. Rev. X* 5, 031023 (2015).
- Zhang, C.-L. et al. Signatures of the Adler–Bell–Jackiw chiral anomaly in a Weyl fermion semimetal. *Nat. Commun.* 7, 10735 (2016).
- Spivak, N. Z. & Andreev, A. V. Magnetotransport phenomena related to the chiral anomaly in Weyl semimetals. *Phys. Rev. B* 93, 085107 (2016).
- Liang, S. et al. Experimental tests of the chiral anomaly magnetoresistance in the Dirac-Weyl semimetals Na₃Bi and GdPtBi. *Phys. Rev. X* 8, 031002 (2018).
- 9. Li, Q. et al. Chiral magnetic effect in ZrTe₅. Nat. Phys. 12, 3648 (2016).
- 10. Li, H. et al. Negative magnetoresistance in Dirac semimetal Cd_3As_2 . Nat. Commun. 7, 10301 (2016).
- Guo, S. T. et al. Large transverse Hall-like signal in topological Dirac semimetal Cd₃As₂. Sci. Rep. 6, 27487 (2016).
- Li, Y. et al. Field-induced resistivity plateau and unsaturated negative magnetoresistance in topological semimetal TaSb₂. *Phys. Rev. B* 94, 121115(R) (2016).
- Li, Y. P. et al. A negative magnetoresistance in topological semimetals
 of transition-metal dipnictides with nontrivial Z2 indices. Preprint at
 https://arxiv.org/abs/1603.04056 (2016).
- 14. Luo, Y. K. et al. Anomalous electronic structure and magnetoresistance in TaAs₂. Sci. Rep. **6**, 27294 (2016).
- Shen, B., Deng, X. Y., Kotliar, G. & Ni, N. Fermi surface topology and negative longitudinal magnetoresistance observed in the semimetal NbAs₂. *Phys. Rev. B* 93, 195119 (2016).
- Baker, D. R. & Heremans, J. P. The linear geometrical magnetoresistance effect: influence of geometry and material composition. *Phys. Rev. B* 59, 13927 (1999).
- Hu, J. S., Rosenbaum, T. F. & Betts, J. B. Current jets, disorder, and linear magnetoresistance in the silver chalcogenides. *Phys. Rev. Lett.* 95, 186603 (2005).

- Li, Y. et al. Negative magnetoresistance in Weyl semimetals NbAs andNbP: intrinsic chiral anomaly and extrinsic effects. Front. Phys. 12, 127205 (2017).
- dos Reis, R. D. et al. On the search for the chiral anomaly in Weyl semimetals: the negative longitudinal magnetoresistance. *New J. Phys.* 18, 085006 (2016).
- Noothoven van Goor, J. M. Donors and Acceptors in Bismuth Philips Research Report Suppl. 4 (Philips, 1971).
- Jin, H. et al. The phonon-induced diamagnetic force and its effect on the lattice thermal conductivity. Nat. Mater. 14, 601–606 (2015).
- Das, K. & Agarwal, A. Thermal and gravitational chiral anomaly induced magneto-transport in Weyl semimetals. *Phys. Rev. Res.* 2, 013088 (2020).
- Gallo, C. F., Chandrasekhar, B. S. & Sutter, P. H. Transport properties of bismuth single crystals. J. Appl. Phys. 34, 144–152 (1963).
- Andreev, A. V. & Spivak, B. Z. Longitudinal negative magnetoresistance and magnetotransport phenomena on conventional and topological conductors. *Phys. Rev. Lett.* 120, 026601 (2018).
- Schindler, C. et al. Anisotropic electrical and thermal magnetotransport in the magnetic semimetal GdPtBi. Phys. Rev. B 101, 125119 (2020).
- Gooth, J. et al. Experimental signatures of the mixed axial–gravitational anomaly in the Weyl semimetal NbP. Nature 547, 324–327 (2017).
- Tolman, R. C. & Ehrenfest, P. Temperature equilibrium in a static gravitational field. *Phys. Rev.* 36, 1791–1798 (1930).
- Luttinger, J. M. Theory of thermal transport coefficients. Phys. Rev. 135, A1505–A1514 (1964).
- Hsieh, D. et al. A topological Dirac insulator in a quantum spin Hall phase. Nature 452, 970–974 (2008).
- Vandaele, K., Otsuka, M., Hasegawa, Y. & Heremans, J. P. Confinement effects, surface effects, and transport in Bi and Bi_{1-x}Sb_x semiconducting and semimetallic nanowires. *J. Phys. Condens. Matter* 30, 403001 (2018).
- Liu, Y. & Allen, R. E. Electronic structure of the semimetals Bi and Sb. Phys. Rev. B 52, 1566–1577 (1995).
- Cucka, P. & Barrett, C. S. The crystal structure of Bi and of solid solutions of Pb, Sn, Sb and Te in Bi. Acta Crystallogr. 15, 865–872 (1962).
- Mendez, E. E., Misu, A. & Dresselhaus, M. S. Pressure-dependent magnetoreflection studies of Bi and Bi_{1-x}Sb_x alloys. *Phys. Rev. B* 24, 639–648 (1981).
- Brandt, N. B., Svistova, E. A. & Semenov, M. V. Electron transitions in antimony-rich bismuth-antimony alloys in strong magnetic fields. Sov. Phys. JETP 32, 238 (1971).
- Şahin, C. & Flatté, M. E. Tunable giant spin hall conductivities in a atrong spin-orbit semimetal: Bi_{1-x}Sb_x. Phys. Rev. Lett. 114, 107201 (2015).
- Cohen, M. H. & Blount, E. I. The g-factor and de Haas-van Alphen effect of electrons in bismuth. *Philos. Mag.* 5, 115–126 (1960).
- 37. Smith, G. E., Baraff, G. A. & Rowell, J. M. Effective g-factor of electrons and holes in bismuth. *Phys. Rev.* 135, A1118 (1964).
- Vecchi, M. P., Pereira, J. R. & Dresselhaus, M. S. Anomalies in the magnetoreflection spectrum of bismuth in the low-quantum-number limit. *Phys. Rev. B* 14, 298–317 (1976).
- Heremans, J. P., Shayegan, M., Dresselhaus, M. S. & Issi, J.-P. High magnetic field thermal conductivity measurements in graphite intercalation compounds. *Phys. Rev. B* 26, 3338–3346 (1982).
- Kagan, V. D. & Red'ko, N. A. Phonon thermal conductivity of bismuth alloys. Sov. Phys. JETP 73, 664–671 (1991).
- Argyres, P. N. & Adams, E. N. Longitudinal magnetoresistance in the quantum limit. *Phys. Rev.* 104, 900–908 (1956).

Publisher's note Springer Nature remains neutral with regard to jurisdictional claims in published maps and institutional affiliations.

© The Author(s), under exclusive licence to Springer Nature Limited 2021

Methods

We studied five samples of nominal composition Bi₈₉Sb₁₁, labelled 1-4 and 6, one Bi₈₅Sb₁₅ and one Bi₉₅Sb₅ sample, cut from four separate single crystals. The Bi₈₅Sb₁₅ (sample 5) and Bi₈₉Sb₁₁ (samples 1 and 6) were grown in-house by the TMZ technique (see Supplementary Information); the Bi₉₅Sb₅ was grown in-house by the Bridgeman method and the Bi₈₉Sb₁₁ (samples 2-4) was grown by Noothoven van Goor using the Czochralski method²⁰. Table 1 summarizes the sample compositions and purpose. We checked the compositional uniformity of the TMZ crystal centres by X-ray diffraction (see Supplementary Information). The $Bi_{89}Sb_{11}$ crystal composition (providing sample 1) was 10.5 ± 0.5 at.%, and the compositional uniformity was interpolated from that of the crystal to better than 0.1% across the sample size. The $Bi_{85}Sb_{15}$ crystal composition was 15.1 ± 0.7 at.%, and the measured sample was uniform to better than 0.1% across the sample size. We measured the low-field Hall effect and resistivity (see Supplementary Information) of separate TMZ crystal pieces, given in Fig. 2a,b. The Hall effect polarity switched from n-type to p-type, indicating almost complete charge-carrier freeze-out. Because Bi and Sb are isoelectronic, achieving freeze-out does not require the exquisite stoichiometric control needed for compound semiconductors, but the starting materials required in-house zone refinement because we could not reach carrier concentrations <10¹⁷ cm⁻³ with 99.999% pure commercial materials. Three cuts (samples 2, 3, 4) of a separate Czochralski crystal piece showed a κ_{zz} increase in field and had electron densities and mobilities of 8×10^{18} cm⁻³ and $1,050\,\mathrm{cm^2\,V^{-1}\,s^{-1}}$ at 300 K, which froze out to $1.4\times10^{16}\,\mathrm{cm^{-3}}$ and $2\times10^4\,\mathrm{cm^2\,V^{-1}}$ s⁻¹ at 12 K. Van Goor determined the composition to be 12%; X-ray diffraction measurements similar to those on the TMZ crystal give 11.3 ± 0.7 at.%.

Thermal conductivity was measured along the <001> crystal direction with the steady-state method in the high-vacuum (10 $^{-6}$ Torr), radiation-shielded environment of a Quantum Design Physical Property Measurement System (PPMS) sample chamber. The heat source was a resistive heater (Omega Engineering, 120 Ω strain gauge) bonded to an Al₂O₃ plate heat spreader. The heat sink, also an Al₂O₃ plate, was glued to the sample platform of a PPMS's puck. The heat source and sink were bonded to the cleaved sample top and bottom using GE varnish to ensure these surfaces were short circuit free. The thermometers were fabricated thermocouples of 25-µm-diameter copper-Constantan couples. The thermometers contacted the sample at different positions along the temperature gradient with epoxy. We conducted measurements at discrete temperatures between 10 K and 300 K. The sample assembly was stabilized thermally at each discrete temperature for 30 minutes before measurement. Magnetothermal conductivity was measured in a sweeping-down magnetic field from 9T to -9T in the PPMS, with sweeping rate of 5 mT s⁻¹. Control software was programmed using LabVIEW. Longitudinal MR measurements $\rho_{zz}(H_z)$ were carried out on sample 6, which was designed with a long, thin geometry $(3 \times 0.4 \times 0.6 \,\mathrm{mm}^3)$ with voltage probe wires attached along the spine of the sample⁸ to minimize current jetting. This, and the fact that the magnetic field alignment was controlled to ~0.1°, minimizes the geometrical MR effects. Its surface was etched to smooth out the surface damage from cutting.

The thermal conductivity measurement error is dominated by the sample geometry uncertainty, of the order of 10%, and the thermocouple calibration. Heat

losses were calculated from the measured instrumental heat leaks, which vary with temperature but are of the order of mW K $^{-1}$ above 200 K, much smaller than the thermal conductance of the sample. The copper–Constantan thermocouples were calibrated in-field using a thermal conductivity measurement on a glass sample (see Supplementary Information). We presumed, in the data treatment, that they have no magnetic field dependence. As measured, the field dependence up to 7T was <2% down to 80 K and <5% down to 34 K, but as much as 10% at 16 K, the lowest reported κ_{zz} temperature. Thus, all data uncertainty reported in Figs. 3 and 4 above 40 K is better than 14%, representing the aggregate of thermocouple calibration uncertainty and heat losses.

For angular-dependent magnetothermal conductivity measurements (see Supplementary Information), an angle between the temperature gradient and the magnetic field was created with a prefabricated, solid copper wedge at a desired angle. The copper wedge was treated as an additional set of thermal and contact resistances in the data analysis.

Data availability

The data generated and analysed in this study are available within the paper and its Supplementary Information. Further data are available from the corresponding author on reasonable request.

Acknowledgements

This work was supported by CEM and NSF MRSEC under grant numbers DMR-2011876 (to D.V., W.Z., N.T., J.P.H.) and DMR-1420451 (all authors). The authors acknowledge useful discussions with M. A. H. Vozmediano. R. Ripley edited the text and contributed to the illustrations.

Author contributions

The experiments were designed and carried out by D.V. and J.P.H. The theory was carried out by W.Z., C.Ş., M.E.F., N.T. and J.P.H. All contributed to the integration of theory and experiment and in writing the manuscript.

Competing interests

The authors declare no competing interests.

Additional information

Supplementary information The online version contains supplementary material available at https://doi.org/10.1038/s41563-021-00983-8.

Correspondence and requests for materials should be addressed to J.P.H.

Peer review information *Nature Materials* thanks Kamran Behnia, Qiang Li, Binghai Yan and the other, anonymous, reviewer(s) for their contribution to the peer review of this work.

 $\textbf{Reprints and permissions information} \ is \ available \ at \ www.nature.com/reprints.$